

Hierarchical search method for gravitational waves from stellar-mass binary black holes in noisy space-based detector data

Yao Fu¹, Yan Wang^{1,*} and Soumya D. Mohanty^{2,3,†}

¹*National Gravitation Laboratory, MOE Key Laboratory of Fundamental Physical Quantities Measurements,
Department of Astronomy and School of Physics,*

Huazhong University of Science and Technology, Wuhan 430074, China

²*Department of Physics and Astronomy, University of Texas Rio Grande Valley, Brownsville, Texas 78520, USA*

³*Department of Physics, IIT Hyderabad, Kandi, Telangana-502284, India*

(Dated: February 4, 2025)

Future space-based laser interferometric detectors, such as LISA, will be able to detect gravitational waves (GWs) generated during the inspiral phase of stellar-mass binary black holes (SmbBHs). These detections contain a wealth of important information concerning astrophysical formation channels and fundamental physics constraints. However, the detection and characterization of GWs from SmbBHs poses a formidable data analysis challenge, arising from the large number of wave cycles that make the search extremely sensitive to mismatches in signal and template parameters in a likelihood-based approach. This makes the search for the maximum of the likelihood function over the signal parameter space an extremely difficult task, with grid-based deterministic global optimization methods becoming computationally infeasible. We present a data analysis method that addresses this problem using both algorithmic innovations and hardware acceleration driven by Graphics Processing Units (GPUs). The method follows a hierarchical approach in which a semi-coherent \mathcal{F} -statistic is computed with different numbers of frequency domain partitions at different stages, with multiple particle swarm optimization (PSO) runs used in each stage for global optimization. An important step in the method is the judicious partitioning of the parameter space at each stage to improve the convergence probability of PSO and avoid premature convergence to noise-induced secondary maxima in the semi-coherent \mathcal{F} -statistic. The hierarchy of stages confines the semi-coherent searches to progressively smaller parameter ranges, with the final stage performing a search for the global maximum of the fully-coherent \mathcal{F} -statistic. We test our method on 2.5 years of a single LISA time delay interferometry (TDI) combination and find that for an injected SmbBH signal with a signal-to-noise ratio (SNR) between ≈ 11 and ≈ 14 , the method can estimate (i) the chirp mass with a relative error of $\lesssim 0.01\%$, (ii) the time of coalescence within ≈ 100 sec, (iii) the sky location within ≈ 0.2 deg², and (iv) orbital eccentricity at a fiducial signal frequency of 10 mHz with a relative error of $\lesssim 1\%$.

I. INTRODUCTION

Since the first direct detection of a gravitational wave (GW) signal from a stellar-mass binary black hole (SmbBH) merger, GW150914 [1], the twin LIGO observatories [2] in coordinated observations with the Virgo [3] and KAGRA [4] detectors have recorded nearly 100 events [5–8] during the first three observing runs (O1 to O3). Due to a lower frequency bound on the sensitive bandwidth of ground-based detectors arising from seismic noise, all observed signals have frequencies higher than ≈ 20 Hz, which corresponds to the late inspiral, and merger phases of stellar-mass binary systems lasting for a ~ 1 min or less. Even with third-generation instruments in the future, such as the Einstein Telescope [9] and Cosmic Explorer [10], ground-based detection of GW signals will ultimately be limited to $\gtrsim 1$ Hz due to gravity gradient noise [11]. Observations of GW signals in the sub-Hz to millihertz range must necessarily use space-based detectors, projected to be operational in the next

decade starting with the launch of the Laser Interferometer Space Antenna (LISA) [12]. At around the same time, the proposed TianQin [13, 14] and Taiji [15, 16] (or one of them) may also join LISA to provide a network of space-based GW detectors that will have a significantly higher combined capability than any of the individual ones [17–20].

LISA will be sensitive to GW signals from a variety of sources in the millihertz range [21, 22], such as galactic compact binaries, extreme-mass-ratio inspirals (EMRIs), supermassive binary black hole mergers, SmbBHs, intermediate-mass binary black holes, and possibly the stochastic background from phase transitions and cosmic strings in the early Universe. Of particular interest to this paper is the fact that, complementary to ground-based detectors, LISA will be able to detect GWs in the early inspiral phase of SmbBHs in the chirp mass range $10 - 100 M_{\odot}$. It is expected that we will observe multiple SmbBHs [23–26] throughout the mission lifetime of LISA and when combined with other proposed space-based GW detectors, such as TianQin [13, 14], Taiji [15, 16], and DECIGO [27, 28], the number of detectable SmbBHs will be further increased [29].

Signals from SmbBHs will contain rich information, which will allow us to study their astrophysical forma-

* ywang12@hust.edu.cn

† soumya.mohanty@utrgv.edu

tion channels [30–33] and constrain fundamental physics theories [34–37]. With a reasonable accuracy in the predicted time of coalescence of an SmBBH system that has a lifetime to merger of a few years, space-based detectors will be able to provide alerts to both ground-based GW detectors as well as electromagnetic observatories, enabling multi-wavelength and multi-messenger observations [23, 38–40] of such events.

However, in order to realize the rich scientific prospects outlined above we have to first overcome the major data analysis challenges [26] posed by the detection and parameter estimation of SmBBHs signals. Unlike ground-based detectors, SmBBH signals will persist in the sensitive frequency range of space-based detectors for several years, spanning more than 10^5 wave cycles. This makes a matched filter-based search extremely sensitive to mismatches in the parameters of the signal and the templates, requiring an estimated $(10^{30} - 10^{40})$ [26] templates to cover the entire signal parameter space. In addition, each template, for 2.5 years of observations with a sampling interval of 10 seconds, will require $\approx 10^7$ samples, making the evaluation of each matched filter output computationally expensive. In fact, the computational cost associated with SmBBH signals is comparable to that of the more widely known problem of matching filter-based search for EMRI signals [41–43] and arises from essentially the same causes, namely, low amplitude signals lasting over many cycles requiring long integration times to accumulate sufficient signal-to-noise ratio (SNR).

Several studies have been conducted to assess the SmBBH data analysis challenge or propose exploratory methods to address it. For example, in [29], the Fisher information matrix was used to evaluate the parameter estimation accuracy of SmBBHs for LISA. As shown in [44], archival searches can uncover many low SNR GW signals in LISA data. In general, methods that have been proposed so far for SmBBH searches have strong underlying assumptions: In [44, 45], the signal parameter search space is significantly restricted, while the performance of the methods in [46–48] have only been studied for noiseless data.

In this paper, we present a data analysis method based on a hierarchical approach enabled by Particle Swarm Optimization (PSO) [49–51] that overcomes some of the above limitations and can search for SmBBH signals over a wide parameter range in the presence of noise, thus significantly advancing the state-of-the-art in this problem. PSO is a stochastic global optimization method that has been applied successfully to a wide range of GW data analysis problems [52–56], and proves to be highly effective in addressing the present problem too. The hierarchical search is comprised of several stages of semi-coherent searches, inspired by the ones used extensively in continuous GW searches [57–59] with ground-based detectors, that are terminated by a fully coherent one. An important feature of our method is the use of parameter space partitioning at each stage to avoid premature convergence to secondary noise-induced maxima of the

semi-coherent search statistic and improve the convergence of PSO to its global maximum. In addition, we use multiple PSO runs at each stage and in each partition to further improve its performance.

A hierarchical search has been investigated in [60] for the case of noiseless data. Our method differs significantly in several aspects, such as the use of parameter space partitioning, maximization over all extrinsic parameters in the semi-coherent log-likelihood functions, and multiple PSO runs. We note that the problem of secondary maxima induced by noise is one of the major challenges in this search that does not appear in noiseless data.

The rest of the paper is organized as follows. Sec. II describes in detail the search statistic. Sec. III provides an overview of the hierarchical search method and its implementation in this paper. Sec. IV describes how we accelerate our code with the frequency-domain response of the detector and GPU-based parallelization. In Sec. V, we present our main results on the performance of the method using simulated data realizations. Our conclusions and discussion of future improvements are presented in Sec. VI. Several technical details have been relegated to two appendices. Throughout this paper, we work in natural units in which $G = c = 1$.

II. \mathcal{F} -STATISTIC AND SEMI-COHERENT SEARCH

In this section, we provide a brief overview of the Generalized Likelihood Ratio Test (GLRT) formalism, commonly called the fully-coherent \mathcal{F} -statistic [61] in GW data analysis, along with our hierarchical search scheme based on the semi- and fully-coherent \mathcal{F} -statistic.

A. Fully-coherent \mathcal{F} -statistic

The data from a space-based detector such as LISA consists of a set of time series $s = \{s^I(t)\}$, $t \in [0, T]$, where I denotes a specific time-delay interferometry (TDI) combination [62, 63] used to suppress laser frequency noise. Commonly used TDI combinations are the Michelson combinations $I \in \{X, Y, Z\}$ and combinations called $\{A, E, T\}$ that have mutually independent noise of instrumental origin [64].

The detection of GW signals in noise requires deciding between the null hypothesis H_0 , namely, the data s does not contain a GW signal, and a set of alternative hypotheses, denoted as H_1 , corresponding to the presence of an additive GW signal characterized by parameters Θ . The most commonly used decision rule in searches for parameterized GW signals with theoretically known

waveforms is the GLRT defined as [65]:

$$\Lambda_G = \max_{\Theta} \Lambda(\Theta|s), \quad (1)$$

$$\Lambda(\Theta|s) = \ln \left(\frac{p(s|H_1; \Theta)}{p(s|H_0)} \right), \quad (2)$$

where $\Lambda(\Theta|s)$ is called the log-likelihood ratio, and the joint probability density functions describing the data under the hypotheses H_0 and H_1 (with signal parameters Θ) are denoted by $p(s|H_0)$ and $p(s|H_1; \Theta)$, respectively.

Assuming that the instrumental noise in each TDI combination is a realization of a stationary Gaussian stochastic process and that the TDI combinations chosen have mutually independent noise,

$$\Lambda(\Theta|s) = \sum_I \left[\langle s^I, h^I(t; \Theta) \rangle_I - \frac{1}{2} \|h^I(t; \Theta)\|_I^2 \right]. \quad (3)$$

Here, $h^I(\Theta)$ represents the GW signal, $\langle a, b \rangle_I$ is the noise-weighted inner product defined as [66],

$$\langle a, b \rangle_I = 4 \operatorname{Re} \int_0^{+\infty} \frac{\tilde{a}(f) \cdot \tilde{b}^*(f)}{S_n^I(f)} df, \quad (4)$$

where $\tilde{a}(f)$ and $\tilde{b}(f)$ are the Fourier transforms of continuous time functions $a(t)$ and $b(t)$, respectively, and $S_n^I(f)$ is the one-sided power spectral density (PSD) of the noise. The norm induced by the inner product is denoted as $\|a\|_I^2 = \langle a, a \rangle_I$. For simplicity, in this work, we only employ the TDI X-combination for which the corresponding one-sided PSD is provided in [12, 62]. While adding data from other combinations is not fundamentally challenging, it increases the computational costs proportionally and exceeds the computational resources available for this study. As such, we drop the use of the TDI combination index I from here on.

In this paper, we employ the restricted post-Newtonian waveform family described in Appendix A that is characterized by a 10-dimensional parameter space. The set of parameters is $\Theta = \{t_c, M_c, \delta_\mu, \theta, \phi, e_0, D_L, \psi, \iota, \phi_c\}$, which denote, starting from t_c , the time of coalescence, the chirp mass, the dimensionless mass difference, the sky location angles ($\theta = \pi/2 - \beta$, $\phi = \lambda$, where λ and β are the ecliptic longitude and ecliptic latitude, respectively), orbital eccentricity at a fiducial signal frequency of 10 mHz, luminosity distance, polarization angle, the angle between the line of sight and the angular momentum direction, and the phase at the coalescence. We consider only the (2, 2) mode of the GW signal and leave the inclusion of higher-order modes arising from significant orbital eccentricity, spin, tidal effects, and other influences, to future work.

The GLRT involves maximizing the log-likelihood ratio defined in Eq. 3 over the space of signal parameters. The value of the global maximum serves as the detection statistic that is compared to a threshold, and if a detection occurs due to the crossing of the threshold, its

location in parameter space provides the Maximum Likelihood Estimate (MLE) of the parameters of the true GW signal. One of the main challenges across many GW data analysis problems, including the SmBBH search, is the extremely high computational cost associated with deterministic methods for solving the global optimization over Θ required in the GLRT.

It is straightforward to show that the response $h(t; \Theta)$ can be written as [61, 67]

$$h(t, \Theta) = \sum_{i=1}^4 a_i A^i(t; \Theta_I), \quad (5)$$

where $\Theta_E = \{a_i\}$, which are time-independent reparameterizations of $\{D_L, \psi, \iota, \phi_c\} \subset \Theta$, comprise the set of extrinsic parameters, while $\Theta_I = \{t_c, M_c, \delta_\mu, \theta, \phi, e_0\}$ form the set of intrinsic parameters. This allows Λ_G to be expressed as

$$\Lambda_G = \max_{\Theta_I} \left(\max_{\Theta_E} \Lambda(\Theta|s) \right). \quad (6)$$

One can analytically maximize $\Lambda(\Theta|s)$ over Θ_E to get the fully-coherent \mathcal{F} -statistic [61, 67],

$$\mathcal{F}(\Theta_I|s) = \max_{\Theta_E} \Lambda(\Theta|s) = \frac{1}{2} N^T(\Theta_I) M^{-1} N(\Theta_I), \quad (7)$$

where,

$$N^i(\Theta_I) = \langle s | A^i(\Theta_I) \rangle, \quad (8)$$

$$M^{ij} = \langle A^i | A^j \rangle, \quad (9)$$

$$a = N^T M^{-1}. \quad (10)$$

The dimensional reduction above from 10 to 6 significantly reduces the difficulty of the global optimization problem. Once the MLE estimates of Θ_I are obtained, the corresponding MLE estimates of Θ_E are obtained as shown in Appendix B.

As mentioned earlier, the global optimization of the fully-coherent \mathcal{F} -statistic over the full astrophysical search range in Θ_I space, called a fully-coherent search, is computationally infeasible if carried out deterministically using a grid of points in this space. Stochastic optimization methods are also likely to fail due to the needle-in-the-haystack problem posed by the extremely small footprint of high values around the global maximum compared to the required search range. A practical solution is to use a hierarchical approach in which the search space is first narrowed down to some promising regions in Θ_I space, making follow up fully-coherent searches in each region computationally feasible. We follow this approach using a semi-coherent version of the \mathcal{F} -statistic as described below. Henceforth, in the following, we use the term search space to refer to the multi-dimensional volume being searched in any one run of PSO while search range refers to the length of the interval along one or more dimensions of this volume.

B. Semi-coherent \mathcal{F} -statistic

The semi-coherent step is inspired by the principal idea behind current continuous wave searches using ground-based GW detectors [57–59]. This is the partitioning of the time domain GW strain data from a detector into smaller segments that are individually subjected to fully coherent searches. Instead of finding just the global optimum in each search, a set of significant locations in Θ_I are found. Different schemes have been proposed and implemented [68–71] for combining these locations into candidates for follow up with fully-coherent searches using longer segment lengths. It should be noted that there are alternative approaches [72] possible in how the initial step of the hierarchy is implemented that do not use the \mathcal{F} -statistic at all. To limit computational costs, the threshold in the initial step of the above types of hierarchical approaches must be set such that the number of false alarms that need to be followed up becomes manageable. As such, semi-coherent searches generally incur a trade-off between available computational resources and loss in detection sensitivity.

The primary motivation for using time-segmentation in ground-based continuous wave searches is the high cost of computing Discrete Fourier Transforms (DFTs) due to the large sampling rate of the data. However, this is not an issue for data from space-based detectors since the number of data samples from the entire mission lifetime of LISA would be $\sim 10^8$, which is just about the size of a ten hours segment from a single LIGO detector sampled at 2048 Hz. Instead, for space-based detectors, the hierarchical approach can be implemented using frequency domain partitioning and this is the approach we follow here.

Let $\tilde{\mathcal{F}}(\Theta_I|s_l)$ denote the \mathcal{F} -statistic function computed using data s_l that is band-limited to $[f_l^{(0)}, f_l^{(1)}]$ and let

$$\begin{aligned}\hat{\mathcal{F}}(\Theta_I) &= \frac{1}{N_{\text{seg}}} \sum_{l=1}^{N_{\text{seg}}} \tilde{\mathcal{F}}_l(\Theta_I), \\ &= \frac{1}{N_{\text{seg}}} \sum_{l=1}^{N_{\text{seg}}} \max_{\Theta_E} \Lambda(\Theta|s_l)\end{aligned}\quad (11)$$

define the semi-coherent \mathcal{F} -statistic, in which N_{seg} is the number of segments. Since the inner product can be computed in the frequency domain following Eq. 4, $\Lambda(\Theta_I|s_l)$ is obtained by simply redefining the inner product for segment l as,

$$\langle s, h \rangle_l = 4 \text{Re} \int_{f_l^{(0)}}^{f_l^{(1)}} \frac{\tilde{s}(f) \cdot \tilde{h}^*(f)}{S_n(f)} df. \quad (12)$$

For continuous GW searches in ground-based detectors, where the signal is nearly monochromatic, the SNR and the number of wave cycles are nearly evenly distributed across time and, hence, the semi-coherent search can use uniform partitioning of the data in the time domain. In contrast, this is not true for SmBBH signals

since the GW power is neither uniformly distributed in time nor in frequency since these are evolving sources. One possible approach is to determine the frequency-domain segment boundaries based on the SNR in each segment. However, as mentioned in [60], this partitioning scheme introduces a dependence of the segment boundaries on the template parameters, necessitating a recalculation of the segment limits for each evaluation of \hat{F} . This can increase program complexity and computation time. Therefore, we opt to compute $f_l^{(1)}$ and $f_l^{(0)}$ by fixing the number of segments for all templates but keeping $f_1^{(0)}$ and $f_{N_{\text{seg}}}^{(1)}$ dependent on some of the intrinsic parameters. In our implementation, these limits are set to be the lowest and highest instantaneous frequencies occurring during the observation period in the template associated with Θ_I .

Unlike the fully coherent case, the calculation of the semi-coherent $\hat{\mathcal{F}}(\Theta_I)$ allows different values of the extrinsic parameters Θ_E for each segment. This reduces the sensitivity of the detection statistic to the intrinsic parameters, and the SNR in each segment is now lowered. However, the profile of the \mathcal{F} -statistic is significantly broadened around the global maximum of the fully-coherent \mathcal{F} -statistic, which reduces the difficulty of the search considerably. Fig. 1 illustrates, in both the absence and presence of noise, the profiles of the semi-coherent \mathcal{F} -statistic with different N_{seg} as a function of the chirp mass M_c . Here, other parameters are set to their true values. Note that $N_{\text{seg}} = 1$ is equivalent to the case of the fully-coherent \mathcal{F} -statistic.

Fig. 1(a) shows how, in the absence of noise, the semi-coherent method expands the width of the peak and absorbs the sharp secondary peaks near the true value of M_c into the main peak. This makes it easier to search for the peak. However, as shown in Fig. 1(b), the peak also becomes less prominent compared to the fluctuations away from the peak caused by noise. Thus, adopting an appropriate N_{seg} according to the type of the GW signal is a key issue in a semi-coherent search.

III. HIERARCHICAL SEARCH PIPELINE

In this section, we provide a brief overview of Particle Swarm Optimization (PSO) and discuss the specific implementation used in this work. This is followed by a description of the search pipeline that uses PSO in multiple stages of a hierarchical search pipeline.

A. PSO

PSO is an iterative stochastic search method for the global maximum of a function $f(x)$, $x \in \mathbb{R}^N$, called the fitness function, over a specified compact subset $D \subset \mathbb{R}^N$ called the search space. [In our case, the fitness function is the semi-coherent \mathcal{F} -statistic (c.f., Eq. 11) and

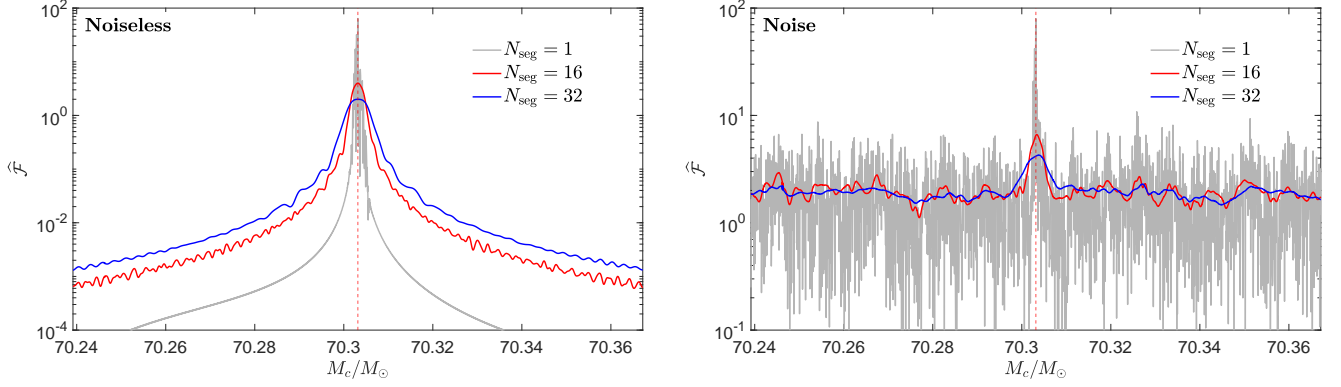


FIG. 1. Comparison of the semi-coherent \mathcal{F} -statistics ($N_{\text{seg}} > 1$) with the fully-coherent \mathcal{F} -statistic ($N_{\text{seg}} = 1$) under different conditions. The true value of the chirp mass, $M_c = 70.3032 M_\odot$, is marked with a red dashed line, while the other parameters are fixed at their true values, and the SNR is 11.3. In the left panel, one can see that, under noiseless condition, the peaks for the semi-coherent \mathcal{F} -statistics are significantly broadened compared to the fully-coherent \mathcal{F} -statistic, which can mitigate the difficulty of the search for the global maximum. However, under noisy conditions, as shown in the right panel, as N_{seg} increases, the peaks become less distinct relative to the fluctuations caused by noise.

the search space is the normalized space of intrinsic parameters Θ_I .] In each iteration, the fitness is sampled at multiple locations and these are updated for the next iteration based on the sampled fitness values. The sampled locations, which are typically fixed in number, are called particles in PSO, with the rules used for updating their positions, called the dynamical equations, stated below. The collection of particles is called a swarm.

Let $x_{i,j}[k]$ denote component j of the position vector x_i of particle $i \leq N_{\text{part}}$ at iteration k . Attached to each particle is a displacement vector $v_i[k]$ (called velocity in PSO terminology) with component j denoted as $v_{i,j}[k]$. The position and velocity are updated as,

$$x_{i,j}[k+1] = x_{i,j}[k] + \min(v_{i,j}[k+1], v_{\text{max}}), \quad (13)$$

$$v_{i,j}[k+1] = w[k]v_{i,j}[k] + c_1 r_1 (p_{i,j}[k] - x_{i,j}[k]) + c_2 r_2 (l_{i,j}[k] - x_{i,j}[k]), \quad (14)$$

where v_{max} limits the maximum step size in any dimension, $w[k]$ denotes a deterministically decaying number called the inertia weight, $c_{1,2}$ are called acceleration constants, $r_{1,2} \sim U([0, 1])$ are independent random variables with uniform distribution over $[0, 1]$, $p_i[k]$ (personal best) is the location with the best fitness in the history of particle i , and $l_i[k]$ (local best) is the best location found in the history of its local neighborhood. (When the local neighborhood includes all the other particles in the swarm, $l_i[k]$ becomes the global best, $g[k]$.) An example of a neighborhood definition is the ring topology [73] in which particle indices are arranged on a circle and a subset of consecutive indices constitutes a neighborhood.

Each of the three terms in Eq. 14 has a special role. The term with the inertial weight, called the inertia term, causes the particle to move past its current location irrespective of its fitness value. This allows the particle to

escape local maxima and contributes to the exploration of the search space. The second term, called the cognitive term, that depends on the personal best can be interpreted as a random force that tries to attract the particle back to a good location that it has already found. The last term, called the social term, that depends on the local best is also a random force that seeks to pull the particle to a good location found by its neighbors. The cognitive and social terms promote exploration around previously found good solutions, a stage of the search called exploitation, but the randomness in these terms prevents too quick a convergence. Thus, the dynamical equations create a trade-off between the exploration and exploitation behavior of the swarm, with the former dominating in the beginning. The use of a local instead of a global best extends the exploration phase by slowing down information flow within the swarm. The inertia weight $w[k]$ is typically allowed to decay linearly with iterations, providing yet another control mechanism for the shift in swarm behavior from exploration to exploitation.

Most PSO implementations work best when the search space D is a hypercube, with component j of x limited to $[a_j, b_j]$. The iterations are commonly initiated with random locations $x_{i,j}[0] \sim U([a_j, b_j])$ and velocities $v_{i,j} \sim U[a_j - x_{i,j}, b_j - x_{i,j}]$. While these initial conditions guarantee that particles will be localized within D in the first position update, it is possible for them to escape D in subsequent iterations. Therefore, boundary conditions need to be specified to handle such particles. Among the many boundary conditions proposed in the literature [74], we choose the let-them-fly condition in which nothing is done to the particles except for setting their fitness to $-\infty$ (in a maximization problem) when they escape D . Similarly, among the diverse termination conditions proposed for PSO, we pick the simplest one in which termination happens once a specified num-

ber of iterations is completed. The final solution for the maximization problem is the global best location and the corresponding fitness value. Although this criterion leads to an excess number of fitness evaluations, it allows load balancing in a parallel implementation of multiple PSO runs and leads to a more efficient utilization of computing resources.

Like most other stochastic heuristics for global optimization, there is no guarantee of convergence (even asymptotically) to the global maximum in PSO but it can be tuned to provide an acceptable probability, P_{success} , of successful convergence to a given region containing the global maximum. This probability can be boosted exponentially by running N_{runs} independent runs of PSO, with statistically independent pseudorandom streams for $r_{1,2}$ and initialization, and picking the best solution across all the runs. The resulting probability of success becomes $1 - (1 - P_{\text{success}})^{N_{\text{runs}}}$, which increases rapidly with N_{runs} even for moderate P_{success} .

Much of the overview provided above is common to several applications of PSO in GW data analysis. In fact, we have adopted the same settings for most of the parameters above as given in [51] except for $N_{\text{part}} = 128$, which is significantly higher than the usual choice of ≈ 40 particles, and different N_{runs} at different stages of the hierarchical search. The large number of particles used here follows from the specific implementation of GPU acceleration used in our code, which requires N_{part} to be a power of 2, and the fact that lower N_{part} values of 32 and 64 did not yield a high probability of successful convergence. As described below, the number of PSO iterations used in the termination criterion varies for the different stages of the hierarchy. The remaining PSO parameters are set to widely used values [73]: $c_1 = c_2 = 2.0$ and $v_{\text{max}} = 0.5$, and because the search range is normalized for PSO, these parameters are dimensionless and the magnitude is independent of the actual search range.

B. Hierarchical search

Despite the significant broadening of the peak in the fitness function, as shown in Fig. 1, it is still much smaller in width than the full search range used in our analysis. In addition, the semi-coherent fitness function is very rugged with multiple local maxima induced by noise in the data. Therefore, PSO would have a low probability of success if it is used over the full search space. To cope with this problem, we divide the search space into smaller regions along certain dimensions, search over the regions independently, and propagate their results in a hierarchical manner through multiple stages in order to progressively narrow down the search around the global maximum of the semi-coherent \mathcal{F} -statistic. The details of this hierarchical pipeline are provided below and illustrated schematically in Fig. 2.

Stage-1: The search range of the parameter t_c is divided into 24 equally wide and contiguous intervals of

length ≈ 0.02 yr. In each interval, 24 independent PSO runs are carried out to search for the global maximum of the semi-coherent \mathcal{F} -statistic using $N_{\text{seg}} = 16$ segments. The best solution among the 24 runs in each region is then recorded, producing a total of 24 candidate locations for the global maximum in the full parameter space. The number of iterations in this step is 8000 for each PSO run.

Stage-2: In this stage, the 24 candidate locations obtained in stage 1 form the centers for new search spaces that are restricted in both t_c and M_c . Based on our experience with different settings, we set the size of each restricted range to 0.01 yr along t_c and $0.6 M_\odot$ along M_c , while keeping the search ranges for all other parameters the same as in stage 1. Therefore, the size of the search spaces in the Stage 2 is two orders of magnitude smaller than in the Stage 1. Each of the 24 regions is now searched with 8 PSO runs and the single best solution from all these $24 \times 8 = 192$ runs is propagated to the next stage. The number of PSO iterations and N_{seg} for semi-coherent \mathcal{F} -statistic remain the same as in stage 1. The single solution provides a candidate location in a search space that is restricted in t_c and M_c but unrestricted in all other parameters.

Stage-3: In this stage, the single solution obtained in the previous stage forms the center of narrower search ranges with 0.004 yr for t_c , $0.3 M_\odot$ for M_c , 0.4 rad for θ , 0.4 rad for ϕ , and 0.006 for e_0 . As for δ_μ , due to the relative insensitivity of the semi-coherent \mathcal{F} -statistic to this parameter, we continue to maintain its original search range. Besides restricting the search ranges, we also create a search space centered on $\pi - \theta$, due to a degeneracy of the \mathcal{F} -statistic in θ . Therefore, the size of the search spaces at this time is seven orders of magnitude smaller than in the Stage 1. Each of the two search spaces is now subjected to 48 PSO runs with 15,000 iterations per run. At this point, N_{seg} is set to 1, which means that this stage uses the fully-coherent \mathcal{F} -statistic. The best solution across the two search spaces provides the final estimate of the intrinsic parameters that are then used to obtain the corresponding estimates of the extrinsic parameters following the expressions given in Appendix B.

While we restrict the search ranges for only t_c and M_c in the first two stages, it is conceivable to have a more general scheme in which the search ranges of additional parameters are restricted. However, our experience shows that this is redundant in the first two stages because the semi-coherent \mathcal{F} -statistic is most sensitive to these two parameters and relatively insensitive to the others. Moreover, subdividing the ranges of the parameters increases the computational cost as the number of such parameters goes up. Thus, subdividing the ranges of only t_c and M_c offers a compromise between effectively locating the interesting search space for the latter stages and the overall computational cost of the search. The number of search spaces in the different stages and the number of PSO runs per search space have been obtained empirically based on their effect on the overall perfor-

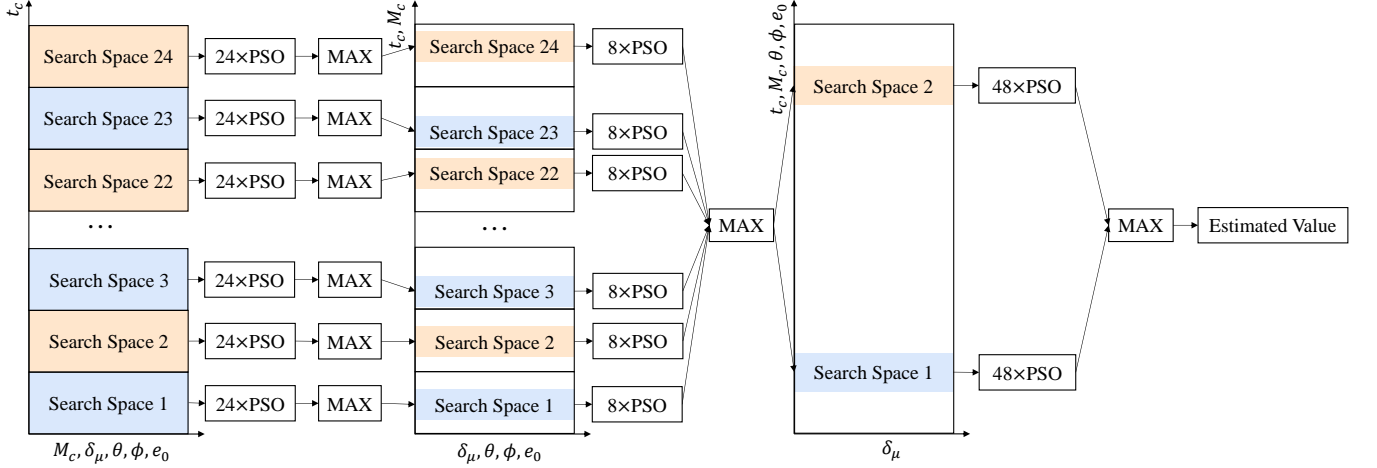


FIG. 2. Flowchart of the hierarchical stages. Each stage is shown by a stack of colored boxes (the boxes are colored with alternating colors for visual clarity). Each stack has two axes: the horizontal and vertical axes are labeled by parameters for which the search space is not subdivided or divided, respectively. Each colored box schematically represents one partition of the search space for the latter set of parameters. In stage-1, starting at the left, the search range of t_c is uniformly divided into 24 contiguous intervals. In stage-2, based on the results of stage-1, the search ranges of both t_c and M_c are narrowed down, while the search ranges of other parameters remain unchanged. In stage-3, the search ranges of all parameters except δ_μ are narrowed down. Each colored box is followed by a box showing the number of PSO runs used in that restricted search space. Each box labeled MAX represents the operation of selecting the best solution out of the PSO runs connected to it. Finally, in stage-3, the two search spaces differ in the range of θ , with the search ranges over all the other parameters kept identical.

mance of the search method. With additional computing resources, these numbers can be increased and the performance can be improved.

It is worth noting that we do not reduce the number of search spaces when going from stage-1 to stage-2. This is because, in the stage-1 search, there is a high probability that secondary maxima induced by noise in search spaces far from the one containing the true parameter have larger values. Therefore, confining the stage-2 search to a subset of the stage-1 search ranges incurs the risk of prematurely converging to secondary maxima. It is preferable to further refine the solution in each search range, as done in stage-2, before deciding to pick the best solution.

IV. EFFICIENT COMPUTATION OF THE SEMI-COHERENT \mathcal{F} STATISTIC

The hierarchical stages described above involve a large number of PSO runs over independent search spaces, with each run requiring a large number of iterations. To mitigate the computational costs involved, we use an efficient calculation of the frequency domain TDI response to a plane GW and implement GPU acceleration of parallelizable steps.

The computationally most expensive step in PSO is the evaluation of the semi-coherent \mathcal{F} -statistic, \hat{F} , for each particle. Calculating \hat{F} involves computing the noise-weighted inner product between the templates and the data, which requires Fourier transforms and consumes a

significant amount of time.

A TDI combination is constructed as a sum of time-delayed single-arm responses. The individual contribution of the GW-induced single-arm response can be written in the following form [75, 76]:

$$x(t) = F(t)h(t + d(t)). \quad (15)$$

Here, $F(t)$ is the time-domain modulation associated with the rotating antenna pattern of the arm and precessional effects in the source orbit evolution. Note that the former depends on the orbit of the detector. For LISA, the orbit used in this study is an analytic approximation, with accuracy extended to second-order eccentricity [77]. While this provides convenience and efficiency, it is worth noting that our work does not depend on it. Numerical orbits with higher precision can also be used, and the evaluation of the detector antenna pattern at specific times requires numerical interpolation using appropriate orders of Chebyshev polynomials, as demonstrated in [78]. $d(t)$ represents the time delay due to the orbital motion of the detector. A GW chirp signal, such as that from an SmBBH inspiral, has a well-defined instantaneous frequency and its Fourier transform can be expressed as [75, 79, 80]:

$$\tilde{h}(f) = A(f)e^{i\Phi(f)}, \quad (16)$$

where $A(f)$ and $\Phi(f)$ can be obtained using the stationary phase approximation. According to [76], for sources where the T_f is much smaller than the timescale of the detector modulation, the Fourier transform of $x(t)$ is well

approximated by:

$$\tilde{x}(f) = T(f)\tilde{h}(f), \quad (17)$$

where

$$T(f) = \sum_{k \geq 0} \frac{(-i)^k}{k!} (T_{Ak})^k F_{T_f, \epsilon} \left[\frac{d^k}{d\tau^k} \left(\frac{F(\tau - d(\tau))}{1 + \dot{d}(\tau)} e^{2i\pi f d(\tau)(1 - \dot{d}(\tau))} \right) \right] (t_f). \quad (18)$$

Here,

$$T_{A1} = \frac{7}{6} \frac{1}{2\pi f}, \quad (19)$$

$$t_f = \frac{1}{2\pi} \frac{d\Phi(f)}{df}, \quad (20)$$

$$T_f^2 = \frac{1}{4\pi} \left| \frac{d^2\Phi}{df^2} \right|, \quad (21)$$

$$\epsilon = -\text{sgn} \left(\frac{d^2\Phi}{df^2} \right) = -1, \quad (22)$$

$$F_{T_f, \epsilon}^N(F)(t) \equiv \frac{1}{2} \sum_{k=0}^N a_{N,k}^\epsilon (F(t + kT_f) + F(t - kT_f)), \quad (23)$$

where $a_{N,k}^\epsilon$ are defined in Appendix 2 of [76]. In this work, all the SmBBHs that we consider have T_f less than 10^6 s, while the modulation timescale of LISA is $\approx 3 \times 10^7$ s, which is consistent with the approximation used in [76] for frequency-domain response in Eq. 17. Thus, even if we set N to zero, and neglect the higher-order terms of $d(t)$ in deriving the frequency-domain response, the match with the approximation-free frequency-domain signal still exceeds 0.999. Using the frequency-domain response in Eq. 17 to compute \tilde{F} not only simplifies the computation since time-domain calculation of the responses are not required but also allows deep parallelization of the calculation.

In the hierarchical method presented in Sec. III, there are several nested parallelizable steps. First, each PSO run can be executed independently. Secondly, within each PSO run, the computation of the semi-coherent \mathcal{F} -statistic for each particle can be carried out in parallel. Finally, in the frequency-domain response, the computations for each frequency can be parallelized. We implement these layers of parallelization using a nested set of hardware elements, starting with nodes of a cluster at the top level, CPU cores at the intermediate level, and GPUs at the deepest level. At present, our parallelization scheme allows the code implementing the hierarchical search described in Sec. III to perform a complete analysis of a single data realization in ≈ 2.5 days using 8

NVIDIA A100 GPUs attached to a single compute node with 48 CPU cores.

In the current state of development of data analysis methods for SmBBHs, the comparison of computational costs is quite difficult because different methods approach the problem with very different objectives (e.g., archival search [44, 45], search in noise free data [46–48, 60], etc.) and the computation time and hardware used are generally not reported in adequate detail. In addition, when comparing computational costs one must account for the SNR of the signal being injected since it affects the performance of the search.

V. RESULTS

In this section, we discuss the results obtained by applying our pipeline to different sets of simulated data.

A. Noiseless data

First, we validate the hierarchical search method on noiseless data. The values of the parameters and corresponding search ranges for the simulated GW signals are given in Table I. Since there is no noise in the data, we can adjust some of the configuration parameters to increase the execution speed. For example, we set $N_{\text{seg}} = 128$ in both stage-1 and stage-2, which significantly reduces the search complexity by broadening the global maximum of the semi-coherent \mathcal{F} -statistic while not incurring any risk of noise-induced secondary maxima. At the same time, we reduce the number of PSO iterations to 2000 for the first two stages and 5000 for the stage-3. Finally, the number of PSO runs per search space was reduced substantially. These adjustments reduced the runtime of the program by a factor of 10 compared to the fiducial settings given in Sec. III.

Table II presents a comparison of the true values with the estimated ones for noiseless data. It can be seen that, except for δ_μ , the intrinsic parameters are recovered with very small relative errors. Part of the error in δ_μ can be attributed to degeneracies between δ_μ and several other parameters in the \mathcal{F} -statistic. To test this hypothesis, we reran the analysis fixing δ_μ to its true value. The corresponding results displayed in Table II show that errors in almost all the parameters are reduced with some of the

TABLE I. The parameters used in the search of noiseless data and their search ranges. The signal amplitude is chosen such that the SNR relative to the instrumental noise has the value shown here. D_L , ι , ψ , and ϕ_c are extrinsic parameters, whose estimated values are obtained from the relationship given in the Appendix B. Hence, they do not have an associated search range.

Parameter	True value	Search range
t_c/yr	3.5000	[3.3, 3.8]
M_c/M_\odot	70.3032	[20, 80]
δ_μ	0.1585	[0, 0.9]
θ/rad	0.7854	[0, π]
ϕ/rad	2.1216	[0, 2π]
$e_0(f_{\text{gw}} = 0.01 \text{ Hz})$	0.0100	[0, 0.05]
D_L/Mpc	920.9084	/
ι/rad	0.5329	/
ψ/rad	1.2501	/
ϕ_c/rad	0.8419	/
SNR	11.3137	/

reductions being significant. This shows that allowing δ_μ to be a free parameter causes errors in other parameters to be compensated by an error in δ_μ . Table II also contains the estimated values of the extrinsic parameters calculated by the procedure in Appendix B. It can be seen that the relative errors in these parameters are orders of magnitude larger than those in the intrinsic parameters. We believe that this is due to some degree of degeneracy within the extrinsic parameters [81]. In the future, using more accurate waveforms that include higher-order modes should improve the accuracy of estimation for the extrinsic parameters [82, 83].

Thus, the analysis of noiseless data validates our code and allows us to proceed to the analysis of realistic noisy data.

B. Noisy data

Within the analysis of noisy data, we considered three separate cases, labeled as cases A, B, and C. Table III provides the values of the true signal parameters in the three cases. The search ranges for all three cases are identical to the ones for the noiseless case listed in Table I. In the following, we discuss the results from these cases in sequence.

The functioning of the hierarchical search is illustrated in Figures 3 to 5 pertaining to Case A. Each figure shows the progression in the localization of the estimated parameter around the true value as one proceeds from stage-1 to stage-3. We see that there is a significant improvement for all parameters except δ_μ . The figures for stage-1 show clearly the effect of secondary maxima induced by noise. For the t_c parameter, the secondary maxima are often larger than the semi-coherent \mathcal{F} -statistic values in the search range containing the true value of this parameter. It is worth noting that the latter may

be just some values found by PSO, not necessarily local maxima at this range. They could be close to secondary maxima, but they could simply result from noise. As discussed earlier in Sec. III, confining the stage-2 search to a subset of stage-1 search spaces based on the semi-coherent \mathcal{F} -statistic values could, therefore, lead to premature convergence. The results for stage-2 show the importance of restricting the search range in M_c along with t_c . We see that, this leads to a significant improvement in the semi-coherent \mathcal{F} -statistic value and that it can often exceed the value at the true location. This is a positive indicator that PSO was able to successfully converge to the global maximum. Finally, we see how the search range is narrowed down by several orders of magnitude at the beginning of stage-3, thus allowing the fully-coherent \mathcal{F} -statistic to be computed successfully.

Tables IV to VI present the estimated parameters and their relative errors for the three cases. It can be seen that the method was able to estimate the intrinsic parameters with very high accuracy. For example, in Case A, the relative error in M_c is less than 0.01% and t_c is determined with an accuracy of ≈ 100 sec. The sky localization is accurate to within 0.2 deg^2 , and the relative errors for eccentricity and chirp mass are less than 1% in all cases. So far, we only provide point estimates for the unknown parameters by MLE, while reporting the uncertainties (error bars) of these estimates (interval estimates) is useful in actual data analysis. One way to obtain error bars in our method is to sample the likelihood function in the restricted parameter space used in Stage 3 using Markov Chain Monte Carlo, or to use a local Gaussian fit to the likelihood function [84]. This will be investigated in our future work.

Case B and Case C differ from Case A primarily in the injected values of the chirp mass. This design allows us to validate our method at different points within its search range. The parameters t_c , θ , ϕ , and e_0 , as well as the extrinsic parameters (except D_L), remain the same as in Case A. The parameter D_L is adjusted to achieve the desired SNRs of the injected signals. As shown in Tables V to VI, the relative errors in the intrinsic parameters are consistent with those in Case A, despite the noise realizations being independent draws based on the LISA instrumental noise PSD.

Moreover, the relative errors in D_L exceed 10% across all three cases with relatively low SNRs, posing a challenge for accurate distance measurement of these sources using GW alone. However, this may be mitigated by the high estimation accuracy achieved in θ and ϕ , making it possible for electromagnetic follow-up to pinpoint their host galaxies. Additionally, predicting the time of coalescence of an SmBBH well before its final merger in high frequency band can provide valuable guidance to ground-based GW detectors. This allows the detectors to be adjusted to their optimal states for this source [36], thereby maximizing the scientific return by combining observations from both high- and low-frequency detectors.

TABLE II. Results of the search in noiseless data. It can be seen that the intrinsic parameters, except δ_μ , are close to their true values. However, there is a considerable error in the extrinsic parameters. This is due to the problem of degeneracy in the GW waveform. Even in a noise-free scenario, obtaining a highly accurate value for these parameters remains challenging. The results of the search when δ_μ is fixed at the true value are also given here, and it can be seen that the error is basically further reduced.

Parameter	True value	Estimated value	Relative error	Estimated value (δ_μ fixed)	Relative error
t_c/yr	3.5000000	3.5000029	0.0000836%	3.4999994	0.0000172%
M_c/M_\odot	70.30316	70.30662	0.00492%	70.30319	0.0000436%
δ_μ	0.1585	0.4784	201%	/	/
θ/rad	0.78540	0.78554	0.0174%	0.78535	0.00621%
ϕ/rad	2.12160	2.12162	0.00128%	2.1214	0.00788%
$e_0(f_{\text{gw}} = 0.01\text{Hz})$	0.01000000	0.00998489	0.151%	0.00999905	0.00947%
D_L/Mpc	920.9084	880.9283	4.34%	895.3753	2.77%
ι/rad	0.5329	0.6088	14.2%	0.5826	9.33%
ψ/rad	1.2501	1.2846	2.76%	1.2831	2.64%
ϕ_c/rad	0.8419	0.2348	72.1%	0.7808	7.26%

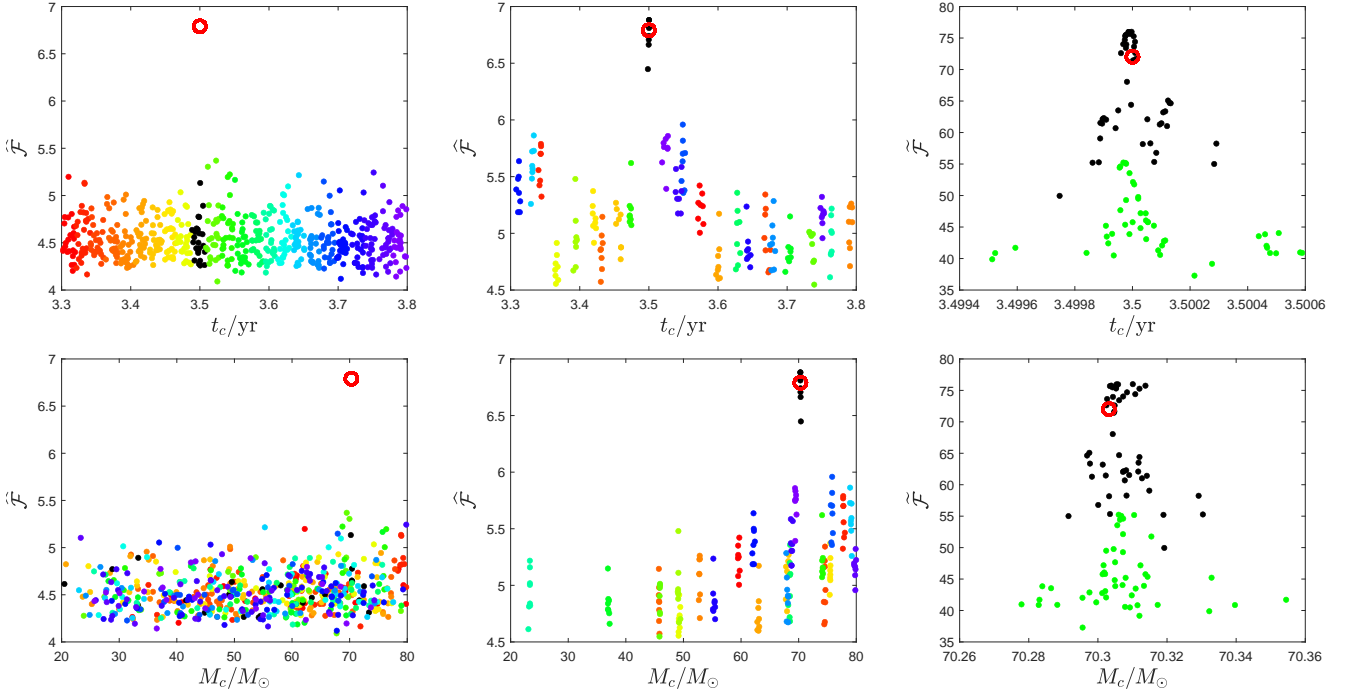


FIG. 3. Part of the PSO results about t_c (top row) and M_c (bottom row). In each panel, the red circle marks the true values of the parameters and their fitness, dots with different colors come from different search ranges of t_c . The black dots represent the PSO results from the range of t_c that encloses its true value. From left to right are stage-1, stage-2, and stage-3.

VI. CONCLUSION

We have presented a hierarchical search method for SmbBH signals in noisy LISA data that shows promising performance for an SNR range of ≈ 11 to ≈ 14 for 2.5 yr of a single TDI combination. The method uses a hierarchy consisting of partitioned parameter search ranges and semi-coherent \mathcal{F} -statistic with different numbers of segments. The search for the global maximum of the semi-coherent \mathcal{F} -statistic in each search range is performed using PSO. By employing frequency-domain

responses and GPU parallel computing to accelerate the code, we were able to efficiently search for single GW signals within a reasonable timeframe of 2.5 days. We validated the reliability of this pipeline using simulated data containing noise based on instrumental design power spectral density of LISA. Our results demonstrate that it is possible to address the data analysis challenges posed by SmbBH signals and produce highly accurate estimates of intrinsic parameters. In particular, the time of coalescence can be localized within ≈ 100 sec and the sky location can be estimated within $\approx 0.2 \text{ deg}^2$, which is more

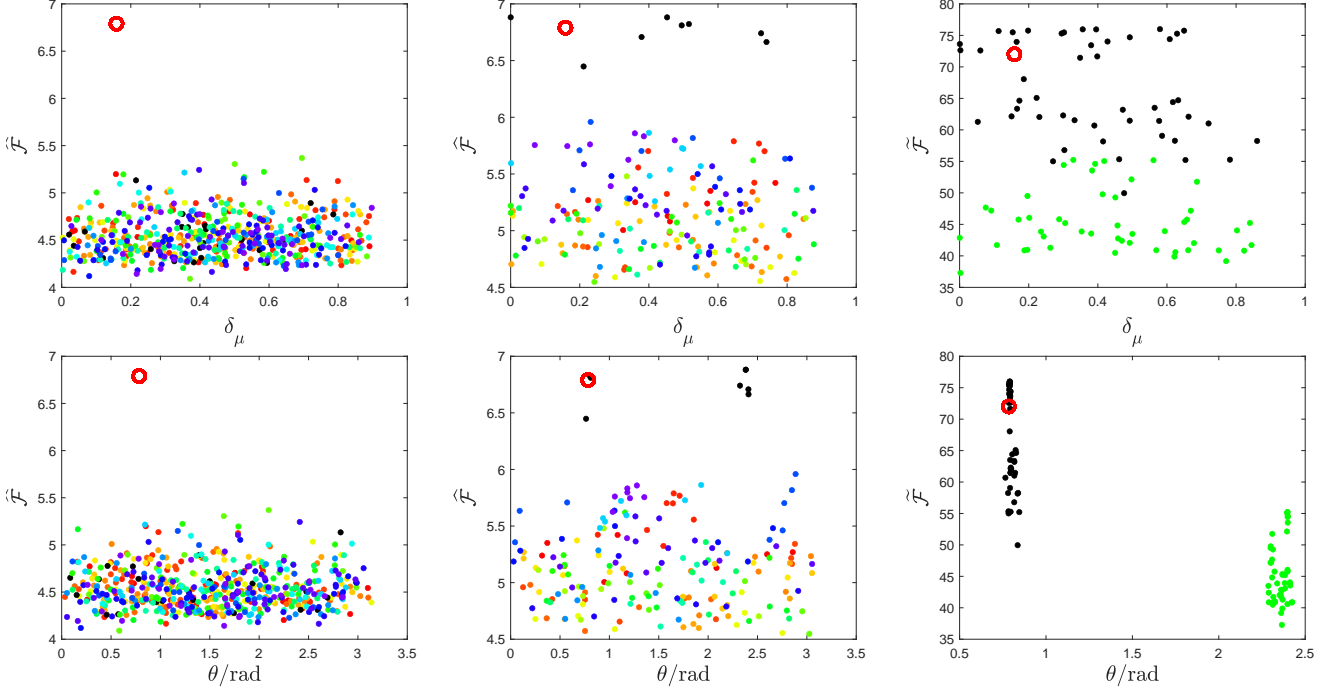
FIG. 4. As in Fig. 3, the PSO results about δ_μ and θ .

TABLE III. The parameters in Case A, Case B, and Case C and their respective search ranges.

Parameter	Case A	Case B	Case C	Search range
t_c/yr	3.5000	3.5000	3.5000	[3.3, 3.8]
M_c/M_\odot	70.3032	54.3572	28.1923	[20, 80]
δ_μ	0.1585	0.0400	0.2485	[0, 0.9]
θ/rad	0.7854	0.7854	0.7854	[0, π]
ϕ/rad	2.1216	2.1216	2.1216	[0, 2π]
$e_0(f_{\text{gw}} = 0.01\text{Hz})$	0.0100	0.0100	0.0100	[0, 0.05]
D_L/Mpc	920.9084	603.5043	123.9608	/
ι/rad	0.5329	0.5329	0.5329	/
ψ/rad	1.2501	1.2501	1.2501	/
ϕ_c/rad	0.8419	0.8419	0.8419	/
SNR	11.3137	11.1723	14.1421	/

than adequate to enable multi-wavelength astronomy for SmBBH sources, and it also opens up the possibility of multi-messenger astronomy if there is an EM counterpart associated with the GW events.

LISA can also measure the orbital eccentricity during inspirals of the SmBBH with a relative error less than 1%, providing the ability to distinguish between their origin from binary star evolution or the dynamical interactions in dense star clusters. However, our waveform model does not include higher-order modes that would be present in a system with high orbital eccentricity. In addition, our waveform model does not include the spins of the individual black holes, which may be important in some cases. We will address these limitations, including the

TABLE IV. Case A search results. The leftmost column lists the true parameters of the injected signal. The second column lists the estimated values found from stage-3 and the third column presents the relative error between the true and estimated values of each parameter.

Parameter	True value	Estimated value	Relative error
t_c/yr	3.500000	3.499997	0.0000899%
M_c/M_\odot	70.3032	70.3101	0.00986%
δ_μ	0.1585	0.5797	265%
θ/rad	0.7854	0.7909	0.696%
ϕ/rad	2.1216	2.1291	0.354%
$e_0(f_{\text{gw}} = 0.01\text{Hz})$	0.010000	0.009953	0.473%
D_L/Mpc	920.9084	397.4851	56.8%
ι/rad	0.5329	1.2719	139%
ψ/rad	1.2501	-0.5077	141%
ϕ_c/rad	0.8419	0.1554	81.5%

use of multiple TDI combinations, in future studies.

Finally, the signals we simulated all merged shortly outside the observation time window, whereas in reality, some sources may merge within the window, while others may merge long after the window. This implies that the search range for the merger time should be expanded, and the problem of multiple sources overlapping should also be addressed.

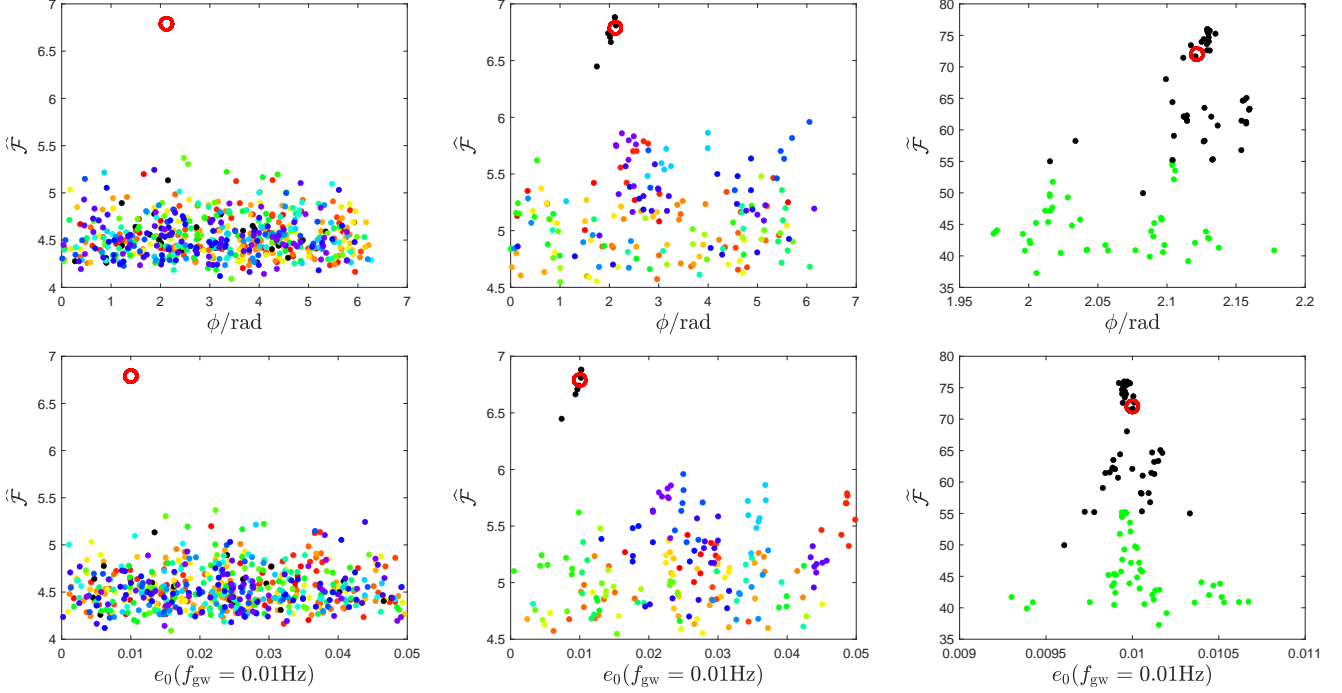


FIG. 5. As in Fig. 3, the PSO results about ϕ and e_0 .

TABLE V. Case B search results. The leftmost column lists the true parameters of the injected signal. The second column lists the estimated values found from stage-3 and the third column presents the relative error between the true and estimated values of each parameter.

Parameter	True value	Estimated value	Relative error
t_c/yr	3.5000000	3.5000142	0.000405%
M_c/M_\odot	54.3572	54.3617	0.00838%
δ_μ	0.0400	0.5721	1330%
θ/rad	0.7854	0.7898	0.558%
ϕ/rad	2.1216	2.1192	0.112%
$e_0(f_{\text{gw}} = 0.01\text{Hz})$	0.01000	0.009970	0.300%
D_L/Mpc	603.5043	513.3089	14.9%
ι/rad	0.5329	0.7259	36.2%
ψ/rad	1.2501	0.4386	64.9%
ϕ_c/rad	0.8419	0.4058	51.8%

TABLE VI. Case C search results. The leftmost column lists the true parameters of the injected signal. The second column lists the estimated values found from stage-3 and the third column presents the relative error between the true and estimated values of each parameter.

Parameter	True value	Estimated value	Relative error
t_c/yr	3.500000	3.5000039	0.0001126%
M_c/M_\odot	28.1923	28.1932	0.00315%
δ_μ	0.07692	0.41195	4355%
θ/rad	0.7854	0.7864	0.129%
ϕ/rad	2.1216	2.1228	0.0575%
$e_0(f_{\text{gw}} = 0.01\text{Hz})$	0.0100	0.009961	0.388%
D_L/Mpc	123.9608	74.1714	40.2%
ι/rad	0.5329	1.1470	115%
ψ/rad	1.2501	-0.3975	132%
ϕ_c/rad	0.8419	0.7437	11.7%

ACKNOWLEDGMENTS

We thank Xin-Chun Hu and Yi-Qian Qian for their helpful discussions. Y.W. gratefully acknowledges support from the National Key Research and Development Program of China (No. 2023YFC2206702 and No. 2022YFC2205201), the National Natural Science Foundation of China (NSFC) under Grant No. 11973024, Major Science and Technology Program of Xinjiang Uygur Autonomous Region (No. 2022A03013-4), and Guangdong Major Project of Basic and Applied Basic Research (Grant No. 2019B030302001). S.D.M. is sup-

ported by U.S. National Science Foundation (NSF) Grant No. PHY-2207935. We acknowledge the High Performance Computing Platform at Huazhong University of Science and Technology for providing computational resources. The authors thank the anonymous referee for helpful comments that have significantly improved our manuscript.

Appendix A: Gravitational Waveforms

In this paper, we employ the restricted post-Newtonian waveforms in the frequency domain, where “restricted” means that we neglect higher-order amplitude modulation and focus only on the post-Newtonian effects in the phase:

$$h(f) = Af^{-7/6}e^{-i\Psi(f)} \quad (\text{A1})$$

where (for $f > 0$):

$$A = -\sqrt{5/24}(M_c^{5/6})/(\pi^{2/3}D_L), \quad (\text{A2})$$

$$\begin{aligned} \Psi(f) = & 2\pi ft_c - \phi_c - \frac{\pi}{4} + \frac{3}{128}(M_c\pi f)^{-5/3} \sum_{k=0}^6 \alpha_k x^{k/2} \\ & - \phi_p(t(f)) - \phi_D(t(f)) + \phi_e(f). \end{aligned} \quad (\text{A3})$$

The details of the parameters, including the coefficients α_k , can be found in [85–88]. In addition, for simplicity, we have omitted certain parameters, such as the spin of the individual black holes, from the waveforms in the current paper, resulting in a total of ten parameters represented by Θ .

Appendix B: Relationships between extrinsic parameters and intrinsic parameters

In Sec. II A, the fully-coherent \mathcal{F} -statistic is obtained by maximizing the log-likelihood ratio function over $\Theta_E = \{a_i\}$, which are time-independent reparameterizations of $\{D_L, \psi, \iota, \phi_c\}$ as follows [89]:

$$\begin{aligned} a_1 &= \frac{1}{D_L} \left(\cos 2\psi \frac{1 + \cos^2 \iota}{2} \cos \phi_c - \sin 2\psi \cos \iota \sin \phi_c \right), \\ a_2 &= -\frac{1}{D_L} \left(\sin 2\psi \frac{1 + \cos^2 \iota}{2} \cos \phi_c + \cos 2\psi \cos \iota \sin \phi_c \right), \\ a_3 &= -\frac{1}{D_L} \left(\cos 2\psi \frac{1 + \cos^2 \iota}{2} \sin \phi_c + \sin 2\psi \cos \iota \cos \phi_c \right), \\ a_4 &= \frac{1}{D_L} \left(\sin 2\psi \frac{1 + \cos^2 \iota}{2} \sin \phi_c - \cos 2\psi \cos \iota \cos \phi_c \right). \end{aligned} \quad (\text{B1})$$

Once the maximum likelihood estimate of the intrinsic parameters (Θ_I) is obtained, a_i can be determined by Eq. 10. Subsequently, the corresponding maximum likelihood estimate of $\{D_L, \psi, \iota, \phi_c\}$ can be obtained by the following relationship,

$$\begin{aligned} D_L &= \frac{2}{A}, \\ \iota &= \arccos \left(\frac{-A_\times}{A_+ + \sqrt{A_+^2 - A_\times^2}} \right), \\ \psi &= \frac{1}{2} \arctan \left(\frac{A_+ a_4 - A_\times a_1}{-(A_\times a_2 + A_+ a_3)} \right), \\ \phi_c &= \arctan \left(\frac{c(A_+ a_4 - A_\times a_1)}{-c(A_\times a_3 + A_+ a_2)} \right), \end{aligned} \quad (\text{B2})$$

where:

$$\begin{aligned} A_+ &= \sqrt{(a_1 + a_4)^2 + (a_2 - a_3)^2} + \sqrt{(a_1 - a_4)^2 + (a_2 + a_3)^2}, \\ A_\times &= \sqrt{(a_1 + a_4)^2 + (a_2 - a_3)^2} - \sqrt{(a_1 - a_4)^2 + (a_2 + a_3)^2}, \\ A &= A_+ + \sqrt{A_+^2 - A_\times^2}, \\ c &= \text{sgn}(\sin(2\psi)). \end{aligned} \quad (\text{B3})$$

-
- [1] B. P. Abbott, R. Abbott, T. Abbott, M. Abernathy, F. Acernese, *et al.*, Observation of gravitational waves from a binary black hole merger, *Physical review letters* **116**, 061102 (2016).
 - [2] J. Aasi, B. Abbott, R. Abbott, T. Abbott, M. Abernathy, *et al.*, Advanced ligo, *Classical and quantum gravity* **32**, 074001 (2015).
 - [3] F. Acernese, M. Agathos, K. Agatsuma, D. Aisa, N. Allemandou, A. Allocca, J. Amarni, P. Astone, G. Balestri,

- G. Ballardin, *et al.*, Advanced Virgo: a second-generation interferometric gravitational wave detector, *Classical and Quantum Gravity* **32**, 024001 (2015), [arXiv:1408.3978 \[gr-qc\]](#).
- [4] K. Somiya, Detector configuration of KAGRA-the Japanese cryogenic gravitational-wave detector, *Classical and Quantum Gravity* **29**, 124007 (2012), [arXiv:1111.7185 \[gr-qc\]](#).
- [5] B. P. Abbott, R. Abbott, T. Abbott, M. Abernathy,

- F. Acernese, *et al.*, Binary black hole mergers in the first advanced ligo observing run, *Physical Review X* **6**, 041015 (2016).
- [6] B. Abbott, R. Abbott, T. Abbott, S. Abraham, F. Acernese, *et al.*, Gwtc-1: a gravitational-wave transient catalog of compact binary mergers observed by ligo and virgo during the first and second observing runs, *Physical Review X* **9**, 031040 (2019).
- [7] R. Abbott, T. Abbott, S. Abraham, F. Acernese, K. Ackley, *et al.*, Gwtc-2: compact binary coalescences observed by ligo and virgo during the first half of the third observing run, *Physical Review X* **11**, 021053 (2021).
- [8] R. Abbott, T. Abbott, F. Acernese, K. Ackley, C. Adams, *et al.*, Gwtc-3: compact binary coalescences observed by ligo and virgo during the second part of the third observing run, *Physical Review X* **13**, 041039 (2023), [arXiv:2111.03606 \[gr-qc\]](#).
- [9] M. Punturo, M. Abernathy, and *et al.*, The Einstein Telescope: a third-generation gravitational wave observatory, *Classical and Quantum Gravity* **27**, 194002 (2010).
- [10] V. Srivastava, D. Davis, K. Kuns, P. Landry, S. Ballmer, M. Evans, E. D. Hall, J. Read, and B. S. Sathyaprakash, Science-driven Tunable Design of Cosmic Explorer Detectors, *Astrophys. J.* **931**, 22 (2022), [arXiv:2201.10668 \[gr-qc\]](#).
- [11] S. Hild, M. Abernathy, F. Acernese, P. Amaro-Seoane, N. Andersson, and *others.*, Sensitivity studies for third-generation gravitational wave observatories, *Classical and Quantum Gravity* **28**, 094013 (2011), [arXiv:1012.0908 \[gr-qc\]](#).
- [12] P. Amaro-Seoane, H. Audley, S. Babak, J. Baker, E. Barausse, P. Bender, E. Berti, P. Binetruy, M. Born, D. Borra, *et al.*, Laser Interferometer Space Antenna, *arXiv e-prints*, [arXiv:1702.00786 \(2017\)](#), [arXiv:1702.00786 \[astro-ph.IM\]](#).
- [13] J. Luo, L.-S. Chen, H.-Z. Duan, Y.-G. Gong, S. Hu, J. Ji, Q. Liu, J. Mei, V. Milyukov, M. Sazhin, *et al.*, TianQin: a space-borne gravitational wave detector, *Classical and Quantum Gravity* **33**, 035010 (2016), [arXiv:1512.02076 \[astro-ph.IM\]](#).
- [14] J. Mei, Y.-Z. Bai, J. Bao, E. Barausse, L. Cai, and *others.*, The TianQin project: Current progress on science and technology, *Progress of Theoretical and Experimental Physics* **2021**, 05A107 (2021), [arXiv:2008.10332 \[gr-qc\]](#).
- [15] W.-R. Hu and Y.-L. Wu, The Taiji Program in Space for gravitational wave physics and the nature of gravity, *National Science Review* **4**, 685 (2017), <https://academic.oup.com/nsr/article-pdf/4/5/685/31566708/nwx116.pdf>.
- [16] W.-H. Ruan, Z.-K. Guo, R.-G. Cai, and Y.-Z. Zhang, Taiji program: Gravitational-wave sources, *International Journal of Modern Physics A* **35**, 2050075 (2020).
- [17] X.-H. Zhang, S.-D. Zhao, S. D. Mohanty, and Y.-X. Liu, Resolving Galactic binaries using a network of space-borne gravitational wave detectors, *Phys. Rev. D* **106**, 102004 (2022), [arXiv:2206.12083 \[gr-qc\]](#).
- [18] Y. Gong, J. Luo, and B. Wang, Concepts and status of Chinese space gravitational wave detection projects, *Nature Astronomy* **5**, 881 (2021), [arXiv:2109.07442 \[astro-ph.IM\]](#).
- [19] A. Torres-Orjuela, S.-J. Huang, Z.-C. Liang, S. Liu, H.-T. Wang, *et al.*, Detection of astrophysical gravitational wave sources by TianQin and LISA, *arXiv e-prints*, [arXiv:2307.16628 \(2023\)](#), [arXiv:2307.16628 \[gr-qc\]](#).
- [20] S.-J. Jin, Y.-Z. Zhang, J.-Y. Song, J.-F. Zhang, and X. Zhang, The Taiji-TianQin-LISA network: Precisely measuring the Hubble constant using both bright and dark sirens, *arXiv e-prints*, [arXiv:2305.19714 \(2023\)](#), [arXiv:2305.19714 \[astro-ph.CO\]](#).
- [21] P. Amaro-Seoane, J. Andrews, M. Arca Sedda, A. Askar, Q. Baghi, *et al.*, Astrophysics with the Laser Interferometer Space Antenna, *Living Reviews in Relativity* **26**, 2 (2023), [arXiv:2203.06016 \[gr-qc\]](#).
- [22] K. G. Arun, E. Belgacem, R. Benkel, L. Bernard, E. Berti, *et al.*, New horizons for fundamental physics with LISA, *Living Reviews in Relativity* **25**, 4 (2022), [arXiv:2205.01597 \[gr-qc\]](#).
- [23] A. Sesana, Prospects for multiband gravitational-wave astronomy after gw150914, *Physical Review Letters* **116**, 231102 (2016).
- [24] K. Kyutoku and N. Seto, Concise estimate of the expected number of detections for stellar-mass binary black holes by elisa, *Monthly Notices of the Royal Astronomical Society* **462**, 2177 (2016).
- [25] K. W. Wong, E. D. Kovetz, C. Cutler, and E. Berti, Expanding the lisa horizon from the ground, *Physical review letters* **121**, 251102 (2018).
- [26] C. J. Moore, D. Gerosa, and A. Klein, Are stellar-mass black-hole binaries too quiet for lisa?, *Monthly Notices of the Royal Astronomical Society: Letters* **488**, L94 (2019).
- [27] S. Sato, S. Kawamura, M. Ando, T. Nakamura, K. Tsubono, A. Araya, I. Funaki, K. Ioka, N. Kanda, S. Moriawaki, *et al.*, The status of DECIGO, in *Journal of Physics Conference Series*, Journal of Physics Conference Series, Vol. 840 (2017) p. 012010.
- [28] S. Kawamura, M. Ando, N. Seto, S. Sato, M. Musha, I. Kawano, J. Yokoyama, T. Tanaka, K. Ioka, T. Akutsu, *et al.*, Current status of space gravitational wave antenna DECIGO and B-DECIGO, *Progress of Theoretical and Experimental Physics* **2021**, 05A105 (2021), [arXiv:2006.13545 \[gr-qc\]](#).
- [29] S. Liu, Y.-M. Hu, J.-d. Zhang, J. Mei, *et al.*, Science with the tianqin observatory: Preliminary results on stellar-mass binary black holes, *Physical Review D* **101**, 103027 (2020).
- [30] A. Nishizawa, E. Berti, A. Klein, and A. Sesana, elisa eccentricity measurements as tracers of binary black hole formation, *Physical Review D* **94**, 064020 (2016).
- [31] K. Breivik, C. L. Rodriguez, S. L. Larson, V. Kalogera, and F. A. Rasio, Distinguishing between formation channels for binary black holes with lisa, *The Astrophysical Journal Letters* **830**, L18 (2016).
- [32] J. Samsing and D. J. D’Orazio, Black hole mergers from globular clusters observable by lisa i: eccentric sources originating from relativistic n-body dynamics, *Monthly Notices of the Royal Astronomical Society* **481**, 5445 (2018).
- [33] D. Gerosa, S. Ma, K. W. Wong, E. Berti, R. O’Shaughnessy, Y. Chen, and K. Belczynski, Multiband gravitational-wave event rates and stellar physics, *Physical Review D* **99**, 103004 (2019).
- [34] K. Chamberlain and N. Yunes, Theoretical physics implications of gravitational wave observation with future detectors, *Physical Review D* **96**, 084039 (2017).
- [35] G. Gnocchi, A. Maselli, T. Abdelsalhin, N. Giacobbo, and M. Mapelli, Bounding alternative theories of gravity with multiband gw observations, *Physical Review D* **100**,

- 064024 (2019).
- [36] R. Tso, D. Gerosa, and Y. Chen, Optimizing ligo with lisa forewarnings to improve black-hole spectroscopy, *Physical Review D* **99**, 124043 (2019).
 - [37] A. Toubiana, S. Marsat, S. Babak, E. Barausse, and J. Baker, Tests of general relativity with stellar-mass black hole binaries observed by lisa, *Physical Review D* **101**, 104038 (2020).
 - [38] S. McGee, A. Sesana, and A. Vecchio, Linking gravitational waves and x-ray phenomena with joint lisa and athena observations, *Nature Astronomy* **4**, 26 (2020).
 - [39] A. Caputo, L. Sberna, A. Toubiana, S. Babak, E. Barausse, *et al.*, Gravitational-wave Detection and Parameter Estimation for Accreting Black-hole Binaries and Their Electromagnetic Counterpart, *Astrophys. J.* **892**, 90 (2020), [arXiv:2001.03620 \[astro-ph.HE\]](#).
 - [40] S. Vitale, Multiband gravitational-wave astronomy: parameter estimation and tests of general relativity with space-and ground-based detectors, *Physical Review Letters* **117**, 051102 (2016).
 - [41] N. J. Cornish, Detection strategies for extreme mass ratio inspirals, *Classical and Quantum Gravity* **28**, 094016 (2011).
 - [42] A. J. Chua, C. J. Moore, and J. R. Gair, Augmented kludge waveforms for detecting extreme-mass-ratio inspirals, *Physical Review D* **96**, 044005 (2017).
 - [43] S. Babak, J. Gair, A. Sesana, E. Barausse, C. F. Sopuerta, *et al.*, Science with the space-based interferometer lisa. v. extreme mass-ratio inspirals, *Physical Review D* **95**, 103012 (2017).
 - [44] B. Ewing, S. Sachdev, S. Borhanian, and B. Sathyaprakash, Archival searches for stellar-mass binary black holes in lisa data, *Physical Review D* **103**, 023025 (2021).
 - [45] H. Wang, I. Harry, A. Nitz, and Y.-M. Hu, Space-based gravitational wave observatories will be able to use eccentricity to unveil stellar-mass binary black hole formation, *Phys. Rev. D* **109**, 063029 (2024), [arXiv:2304.10340 \[astro-ph.HE\]](#).
 - [46] R. Buscicchio, A. Klein, E. Roebber, C. J. Moore, D. Gerosa, E. Finch, and A. Vecchio, Bayesian parameter estimation of stellar-mass black-hole binaries with lisa, *Physical Review D* **104**, 044065 (2021).
 - [47] A. Toubiana, S. Marsat, S. Babak, J. Baker, and T. Dal Canton, Parameter estimation of stellar-mass black hole binaries with lisa, *Physical Review D* **102**, 124037 (2020).
 - [48] X. Lyu, E.-K. Li, and Y.-M. Hu, Parameter Estimation of Stellar Mass Binary Black Holes under the Network of TianQin and LISA, *arXiv e-prints*, [arXiv:2307.12244 \(2023\)](#), [arXiv:2307.12244 \[gr-qc\]](#).
 - [49] J. Kennedy and R. Eberhart, Particle swarm optimization, in *Proceedings of ICNN'95 - International Conference on Neural Networks*, Vol. 4 (IEEE, 1995) pp. 1942–1948.
 - [50] Y. Shi, A modified particle swarm optimizer, in *Proc of IEEE Icc Conference* (1998).
 - [51] S. Mohanty, *Swarm intelligence methods for statistical regression* (CRC Press, 2018).
 - [52] T. S. Weerathunga and S. D. Mohanty, Performance of particle swarm optimization on the fully-coherent all-sky search for gravitational waves from compact binary coalescences, *Phys. Rev. D* **95**, 124030 (2017), [arXiv:1703.01521 \[gr-qc\]](#).
 - [53] M. E. Normandin and S. D. Mohanty, Towards a real-time fully-coherent all-sky search for gravitational waves from compact binary coalescences using particle swarm optimization, *Phys. Rev. D* **101**, 082001 (2020), [arXiv:2002.02150 \[astro-ph.IM\]](#).
 - [54] X.-H. Zhang, S. D. Mohanty, X.-B. Zou, and Y.-X. Liu, Resolving Galactic binaries in LISA data using particle swarm optimization and cross-validation, *Phys. Rev. D* **104**, 024023 (2021), [arXiv:2103.09391 \[gr-qc\]](#).
 - [55] Y. Wang, S. D. Mohanty, and F. A. Jenet, Coherent Network Analysis for Continuous Gravitational Wave Signals in a Pulsar Timing Array: Pulsar Phases as Extrinsic Parameters, *Astrophys. J.* **815**, 125 (2015), [arXiv:1506.01526 \[astro-ph.IM\]](#).
 - [56] Y. Wang and S. D. Mohanty, Pulsar Timing Array Based Search for Supermassive Black Hole Binaries in the Square Kilometer Array Era, *Phys. Rev. Lett.* **118**, 151104 (2017), [arXiv:1611.09440 \[astro-ph.IM\]](#).
 - [57] K. Riles, Searches for continuous-wave gravitational radiation, *Living Reviews in Relativity* **26**, 3 (2023), [arXiv:2206.06447 \[astro-ph.HE\]](#).
 - [58] B. Steltner, M. A. Papa, H.-B. Eggenstein, B. Allen, V. Dergachev, R. Prix, B. Machenschalk, S. Walsh, S. J. Zhu, O. Behnke, *et al.*, Einstein@ home all-sky search for continuous gravitational waves in ligo o2 public data, *The Astrophysical Journal* **909**, 79 (2021).
 - [59] B. Steltner, M. Papa, H.-B. Eggenstein, R. Prix, M. Bensch, B. Allen, and B. Machenschalk, Deep einstein@ home all-sky search for continuous gravitational waves in ligo o3 public data, *The Astrophysical Journal* **952**, 55 (2023).
 - [60] D. Bandopadhyay and C. J. Moore, LISA stellar-mass black hole searches with semicoherent and particle-swarm methods, *Phys. Rev. D* **108**, 084014 (2023), [arXiv:2305.18048 \[gr-qc\]](#).
 - [61] P. Jaranowski, A. Krolak, and B. F. Schutz, Data analysis of gravitational-wave signals from spinning neutron stars: The signal and its detection, *Physical Review D* **58**, 063001 (1998).
 - [62] J. W. Armstrong, F. B. Estabrook, and M. Tinto, Time-Delay Interferometry for Space-based Gravitational Wave Searches, *Astrophys. J.* **527**, 814 (1999).
 - [63] M. Tinto and S. V. Dhurandhar, Time-Delay Interferometry, *Living Reviews in Relativity* **8**, 4 (2005).
 - [64] T. A. Prince, M. Tinto, S. L. Larson, and J. W. Armstrong, Lisa optimal sensitivity, *Phys. Rev. D* **66**, 122002 (2002).
 - [65] S. M. Kay, *Fundamentals of statistical signal processing: estimation theory* (Prentice-Hall, Inc., USA, 1993).
 - [66] L. S. Finn, Detection, measurement, and gravitational radiation, *Phys. Rev. D* **46**, 5236 (1992), [arXiv:gr-qc/9209010 \[gr-qc\]](#).
 - [67] J. Crowder and N. J. Cornish, Solution to the galactic foreground problem for lisa, *Physical Review D* **75**, 043008 (2007).
 - [68] P. R. Brady and T. Creighton, Searching for periodic sources with LIGO. II. Hierarchical searches, *Phys. Rev. D* **61**, 082001 (2000), [arXiv:gr-qc/9812014 \[gr-qc\]](#).
 - [69] C. Cutler, I. Gholami, and B. Krishnan, Improved stack-slide searches for gravitational-wave pulsars, *Phys. Rev. D* **72**, 042004 (2005), [arXiv:gr-qc/0505082 \[gr-qc\]](#).
 - [70] B. Krishnan, A. M. Sintes, M. A. Papa, B. F. Schutz, S. Frasca, and C. Palomba, Hough transform search for continuous gravitational waves, *Phys. Rev. D* **70**, 082001

- (2004), [arXiv:gr-qc/0407001 \[gr-qc\]](#).
- [71] F. Antonucci, P. Astone, S. D'Antonio, S. Frasca, and C. Palomba, Detection of periodic gravitational wave sources by hough transform in the f versus plane, *Classical and Quantum Gravity* **25**, 184015 (2008).
 - [72] S. Dhurandhar, B. Krishnan, H. Mukhopadhyay, and J. T. Whelan, Cross-correlation search for periodic gravitational waves, *Phys. Rev. D* **77**, 082001 (2008), [arXiv:0712.1578 \[gr-qc\]](#).
 - [73] D. Bratton and J. Kennedy, Defining a standard for particle swarm optimization, in *2007 IEEE Swarm Intelligence Symposium* (2007) pp. 120–127.
 - [74] A. Engelbercht, Fundamentals of computational swarm intelligence, University of Pretoria, South Africa (2005).
 - [75] M. Vallisneri, Synthetic LISA: Simulating time delay interferometry in a model LISA, *Phys. Rev. D* **71**, 022001 (2005), [arXiv:gr-qc/0407102 \[gr-qc\]](#).
 - [76] S. Marsat and J. G. Baker, Fourier-domain modulations and delays of gravitational-wave signals, *arXiv e-prints*, [arXiv:1806.10734](#) (2018), [arXiv:1806.10734 \[gr-qc\]](#).
 - [77] N. J. Cornish and L. J. Rubbo, LISA response function, *Phys. Rev. D* **67**, 022001 (2003).
 - [78] M.-Y. Zhou, X.-C. Hu, B. Ye, S. Hu, D.-D. Zhu, X. Zhang, W. Su, and Y. Wang, Orbital effects on time delay interferometry for TianQin, *Phys. Rev. D* **103**, 103026 (2021), [arXiv:2102.10291 \[astro-ph.IM\]](#).
 - [79] L. J. Rubbo, N. J. Cornish, and O. Poujade, Forward modeling of space-borne gravitational wave detectors, *Phys. Rev. D* **69**, 082003 (2004).
 - [80] F. B. Estabrook and H. D. Wahlquist, Response of Doppler spacecraft tracking to gravitational radiation., *General Relativity and Gravitation* **6**, 439 (1975).
 - [81] R. Wang and B. Hu, LitePIG: a lite parameter inference system for the gravitational wave in the millihertz band, *Communications in Theoretical Physics* **75**, 075402 (2023), [arXiv:2208.13351 \[astro-ph.IM\]](#).
 - [82] P. Kumar, J. Blackman, S. E. Field, M. Scheel, C. R. Galley, M. Boyle, L. E. Kidder, H. P. Pfeiffer, B. Szilagyi, and S. A. Teukolsky, Constraining the parameters of gw150914 and gw170104 with numerical relativity surrogates, *Phys. Rev. D* **99**, 124005 (2019).
 - [83] Y. Gong, Z. Cao, J. Zhao, and L. Shao, Including higher harmonics in gravitational-wave parameter estimation and cosmological implications for lisa, *Phys. Rev. D* **108**, 064046 (2023).
 - [84] J. Prasad and T. Souradeep, Cosmological parameter estimation using particle swarm optimization, *Phys. Rev. D* **85**, 123008 (2012).
 - [85] W.-F. Feng, H.-T. Wang, X.-C. Hu, Y.-M. Hu, and Y. Wang, Preliminary study on parameter estimation accuracy of supermassive black hole binary inspirals for TianQin, *Phys. Rev. D* **99**, 123002 (2019), [arXiv:1901.02159 \[astro-ph.IM\]](#).
 - [86] C. Cutler, Angular resolution of the lisa gravitational wave detector, *Phys. Rev. D* **57**, 7089 (1998).
 - [87] A. Królak, K. D. Kokkotas, and G. Schäfer, Estimation of the post-newtonian parameters in the gravitational-wave emission of a coalescing binary, *Phys. Rev. D* **52**, 2089 (1995).
 - [88] A. Buonanno, B. R. Iyer, E. Ochsner, Y. Pan, and B. S. Sathyaprakash, Comparison of post-newtonian templates for compact binary inspiral signals in gravitational-wave detectors, *Phys. Rev. D* **80**, 084043 (2009).
 - [89] J. Crowder and N. J. Cornish, Solution to the galactic foreground problem for LISA, *Phys. Rev. D* **75**, 043008 (2007), [arXiv:astro-ph/0611546 \[astro-ph\]](#).